J. Appl. Comput. Mech., xx(x) (2025) 1-13
DOI: 10.22055/jacm.2025.48638.5385

ISSN: 2383-4536
jacm.scu.ac.ir

Shahid Chamran University of Ahvaz

Journal of Applied and Computational Mechanics

Research Paper

Transfiguration of Random Auxeticity of Programmable Metamaterial: A Kirigami Inspired Approach

Subrata Barman, Simma Bhargava Naidu, Yashwanth Kamasani, Sudip Dey

National Institute of Technology Silchar, Silchar, 788010, India,

Email: subrata21_rs@mech.nits.ac.in (S.B.); simma21_ug@mech.nits.ac.in (S.B.N.); kamasani21_ug@mech.nits.ac.in (Y.K.); sudip@mech.nits.ac.in (S.D.)

Received July 26 2025; Revised October 24 2025; Accepted for publication November 06 2025.
✉ Corresponding author: S. Barman (subrata21_rs@mech.nits.ac.in)

Abstract. This paper presents a comprehensive investigation into the auxetic behavior of a mechanical metamaterial inspired by a Kirigami structure. Through an integrated approach involving finite element analysis (FEA), and Monte Carlo (MC) simulations, the study explores the mechanical response of the metamaterial unit cell and its tessellated configurations. The study confirms the manifestation of a negative Poisson's ratio (NPR) through detailed deformation and stress analyses under compressive loading. The auxetic response is further validated by modeling 2D tessellations in rigid dynamics, demonstrating directional expansion during axial compression and a calculated Poisson's ratio of -0.5386. Analytical models are developed to evaluate angular deformations and Poisson's ratio based on geometric parameters. These models are statistically validated using MC simulation, generating probability distributions of NPR under varied geometric configurations. Sensitivity analyses reveal that the side length is the most influential parameter governing both in-plane and out-of-plane auxetic responses, followed by deformation and extrusion length. Connector length has minimal impact. These findings not only reveal the auxetic nature of the design but also offer critical insights for optimizing structural performance through parameter tuning. The study provides a robust design and analysis of auxetic metamaterials with potential applications in energy ab-sorption, flexible mechanics, and impact-resistant structures.

Keywords: Kirigami, Metamaterial, Auxeticity, Stochastic Analysis, Sensitivity Analysis.

1. Introduction

The field of material science has experienced a transformative shift with the introduction of metamaterials—artificially engineered materials that exhibit exceptional properties not found in natural substances [1-6]. These remarkable attributes arise not from the material's intrinsic composition but from their precisely designed internal architectures. The term "metamaterials," derived from the Greek word meta, meaning "beyond," aptly captures their capability to transcend conventional material limitations [7-12]. Unlike traditional materials, whose behaviours are dictated by their chemical composition, metamaterials derive their properties from structural geometry, allowing for the design of novel functionalities [13]. Metamaterials have revolutionized various domains in science and engineering by enabling control over electromagnetic, acoustic, thermal, and mechanical phenomena [14-18]. These materials have found promising applications in areas such as cloaking devices, vibration damping systems, impact-resistant structures, acoustic insulation, and thermal regulation [19-21]. One of the most intriguing mechanical properties exhibited by some metamaterials is a negative Poisson's ratio (NPR), commonly referred to as auxetic behavior [22-28]. Unlike conventional materials that contract laterally when stretched, auxetic materials expand perpendicular to the applied force, and conversely contract laterally when compressed [29-32]. This unusual behavior offers auxetic materials superior energy absorption, impact resistance, shear resistance, and fracture toughness, making them suitable for advanced engineering applications such as aerospace structures, biomedical implants, protective gear, and morphing devices [33]. Early research efforts focused primarily on two-dimensional geometries, particularly re-entrant honeycombs, and chiral lattices, which provided intuitive and manufacturable routes to achieve NPR behavior [34-38]. These structures demonstrated that by introducing controlled deformations or re-entrant features into the unit cell geometry, auxetic behavior could be successfully induced [39]. Over time, researchers expanded these concepts to three-dimensional structures to improve isotropy and broaden the range of mechanical performance [26, 37, 40].

Kirigami-inspired designs, which are derived from the ancient Japanese art of paper cutting, have recently gained popularity as a powerful means of realizing programmable, reconfigurable metamaterials [41-45]. Sinha and Mukhopadhyay [39] proposed a hybrid metamaterial based on Kirigami that demonstrated stiffness modulation and exhibited multi-directional auxetic behavior with mixed-mode deformation characteristics. Their work showcased the potential for Kirigami-inspired geometries to achieve a combination of positive and negative Poisson's ratios in a single structure. Chen et al. [46] further explored programmable super-elastic Kirigami metallic glasses, emphasizing the tunability of mechanical behavior through patterned cuts and folds. Li et al. [47] developed three-dimensional reconfigurable Kirigami architectures capable of dynamic mechanical transformations. Hou et al. [48] analysed polymorphic honeycombs with gradient rib lengths, offering insight into the structural behavior of auxetic configurations under varying conditions. Qiu et al. [49] proposed self-locking Kirigami panels with a tucked-interleaved pattern that delivered

Published online: November 08 2025

programmable stiffness and enhanced structural integrity under quasi-static loading conditions. These innovations underscored the potential of Kirigami-inspired systems for use in impact resistance, vibration control, and lightweight morphing applications. Ruan et al. [50] presented a hybrid Kirigami design for energy absorption, combining structural tubes with cut-patterns to achieve high energy dissipation and reduced impact forces. Similarly, Lu et al. [51] introduced a programmable 3D morphing mechanism utilizing buckling-induced transformation, highlighting the practical applicability of mechanical metamaterials in adaptive systems such as shape-changing wings and wearable devices. Researchers employed unit-cell-based modeling and finite element simulations to understand and predict the mechanical behavior of origami and Kirigami metamaterials [39, 52]. These methods, often relying on periodic boundary conditions and symmetry considerations, enable efficient analysis and design optimization of metamaterials for targeted mechanical properties. Among the various geometric configurations used to develop NPR metamaterials, the truncated octahedron has emerged as a particularly promising unit cell due to its geometric versatility and tessellation capability [53-55]. Despite its potential, relatively few studies have comprehensively explored truncated octahedron-based designs in the context of auxetic metamaterials. Theoretical and numerical investigations of such three-dimensional configurations remain limited, particularly when considering the interaction between geometric parameters and resulting mechanical properties.

To address this gap, the present study investigates the auxetic behavior of a Kirigami inspired mechanical metamaterial based on the truncated octahedron structure. A detailed three-dimensional CAD model is developed to define the unit cell, incorporating extrusions and connectors to facilitate assembly into one-dimensional and two-dimensional tessellated structures. Finite element simulations are carried out in ANSYS to evaluate the structural response under compressive loading, employing both static structural and rigid body dynamics analyses. Material properties of structural steel are considered, and the effects of geometric variables such as side length, extrusion length, and connector length are systematically studied. Furthermore, analytical formulations are developed to model the deformation angles and calculate Poisson's ratio. To statistically validate the auxetic behavior, the study employs the Monte Carlo method, a probabilistic approach ideal for evaluating systems with geometric variability and uncertainty. Using MATLAB, a Monte Carlo simulation is implemented with 10,000 random samples, allowing a detailed statistical analysis of Poisson's ratio and its sensitivity to key geometric parameters. The resulting probability distribution functions provided insights into the robustness and reliability of the observed auxetic response.

2. Methodology

A truncated octahedron is a convex polyhedral solid characterized by six square faces and eight regular hexagonal faces. It is derived geometrically from a regular octahedron as shown in Fig. 1(a) by truncating its six vertices, effectively removing pyramidal sections from each corner. This transformation increases the number of faces from eight to fourteen, resulting in a structure with thirty-six edges and twenty-four vertices as presented in Fig. 1(b). To design a unit cell suitable for mechanical metamaterials, the truncated octahedron is modified by introducing structural features such as extrusions and connectors, as illustrated in Fig. 1(c). The hexagonal faces (green) are replaced with prismatic extrusions to enable deformability, while the square faces are retained as rigid components (red). This modified geometry is shown in Fig. 2. The surface body thus comprises green extrusions and red connectors, which facilitate rigid joining of multiple unit cells, enabling the construction of one-dimensional (1D) and two-dimensional (2D) tessellated assemblies.

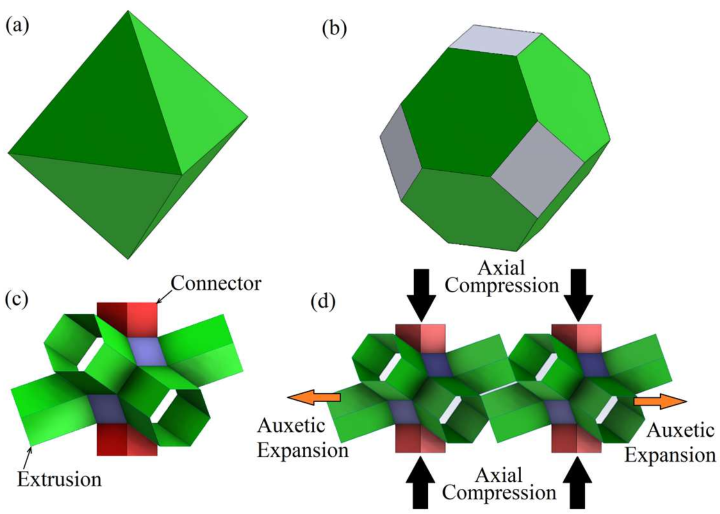

Fig. 1. (a) Octahedral base geometry, (b) truncated octahedral, (c) truncated octahedron with extrusions and connectors representing the metamaterial unit-cell, and (d) schematic presenting auxetic expansion of metamaterial under compressive loading.

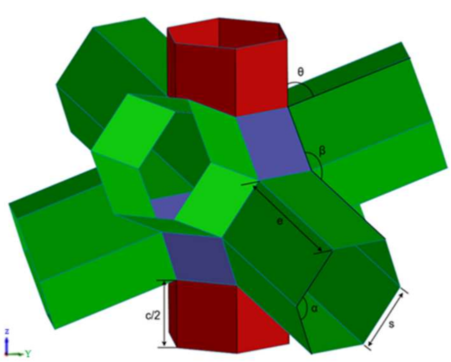

Fig. 2. The unit-cell geometry derived from the truncated octahedron.

Table 1. Geometric and material parameters for symmetric unit cell simulation.

Parameter	Symbol	Value
Side length	*s*	20 mm
Extrusion length	*e*	40 mm
Connector length	*c*	40 mm
Material	–	Structural steel
Density	–	7850 kg/m³
Young's Modulus	–	200 GPa
Poisson's Ratio	–	0.3
Applied Force	–	7000 N → 10000 N

Table 2. Geometric parameters for rigid body dynamics simulations.

Configuration	Side Length (*s*)	Extrusion Length (*e*)	Connector Length (*c*)	Unit Cells
2D Tessellation (Validation)	10 mm	20 mm	20 mm	2
2D Tessellation (Extended)	10 mm	20 mm	20 mm	3

In the 1D tessellation (Fig. 3(a)), unit cells are connected vertically using rigid connectors, while in the 2D tessellation (Fig. 3(b)), horizontal linkages are established using hinged connectors, allowing for relative motion under external loads. During compression, vertical prismatic extrusions of adjacent cells come into contact, enabling load sharing and energy dissipation. Under tension, in-plane extrusions maintain interlocking contact between horizontally adjacent cells, promoting structural coherence and tailored mechanical response.

To investigate the mechanical behavior of the structure, two simulation approaches are adopted in ANSYS:
(i) Static Structural Analysis of a symmetric unit cell, and
(ii) Rigid Body Dynamics Simulation of 2D tessellations.

2.1. Symmetric unit cell analysis

A symmetric unit cell with surface geometry is modelled using quadrilateral shell elements to capture large deformation under applied loading. The material is selected as structural steel. Nonlinear analysis is enabled to account for geometric nonlinearity arising from large deflections. The loading is applied incrementally: first 7000 N, followed by a total of 10,000 N in the second stage. The parameters used for the model are summarized in Table 1.

2.2. Rigid body dynamics for 2D tessellation

To validate the auxetic (negative Poisson's ratio) behavior, Rigid Body Dynamics simulations are conducted for 2D tessellations. Two configurations are considered—one with two-unit cells and another with three-unit cells—for qualitative and statistical analysis of deformation behavior, respectively.

In both cases, the surface body representation is used, consistent with thin-sheet Kirigami designs. The unit cells are treated as rigid, with revolute joints connecting their edges to allow rotational motion. The bottom left connector is fixed using a Remote Displacement constraint (all DOFs = 0), while the top connectors receive a downward displacement of 20 mm to simulate compression. The geometric parameters of the Kirigami-inspired metamaterial, including side length (s = 10 mm), edge length (e = 20 mm), and connector length (c = 20 mm), were carefully selected considering manufacturability, structural stability, and computational feasibility. These dimensions ensure adequate stiffness and geometric integrity under compressive loading while allowing sufficient deformation to exhibit auxetic behavior. Moreover, the millimeter-scale geometry aligns with the feasible resolution limits of laser-cut thin metallic or polymeric sheets, facilitating potential experimental realization. From a simulation standpoint, this geometric configuration offers numerical stability and convergence during finite element and rigid-body dynamics analyses without inducing excessive mesh distortion or computational load. The selected parameters effectively balance mechanical representativeness, physical feasibility, and computational efficiency. The geometric parameters used in both cases are listed in Table 2.

The surface geometry of each face is modelled individually. Revolute joints enable inter-unit rotation, simulating the mechanical response of flexible hinges. Boundary conditions and displacement inputs are consistently applied across both configurations to ensure methodological consistency. The overall research workflow followed in this study is summarized in Fig. 4.

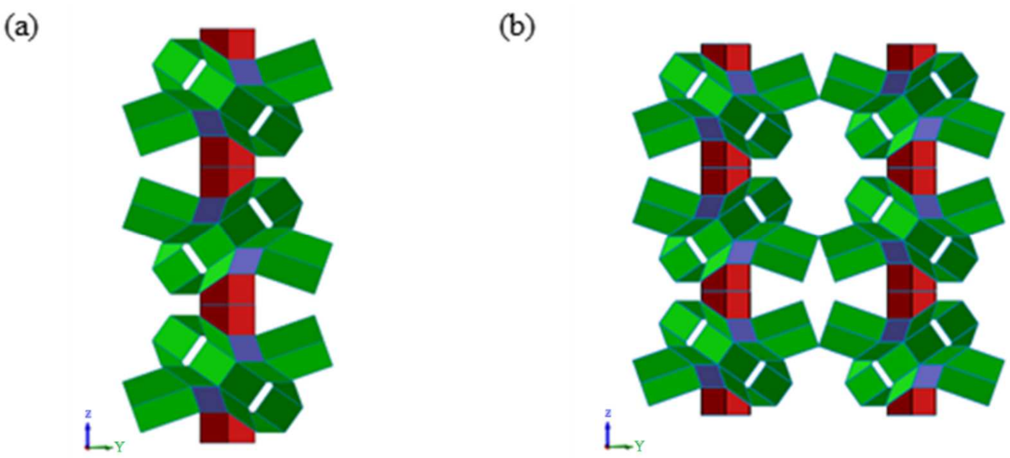

Fig. 3. (a) A one-dimensional tessellation, (b) A two-dimensional tessellation.

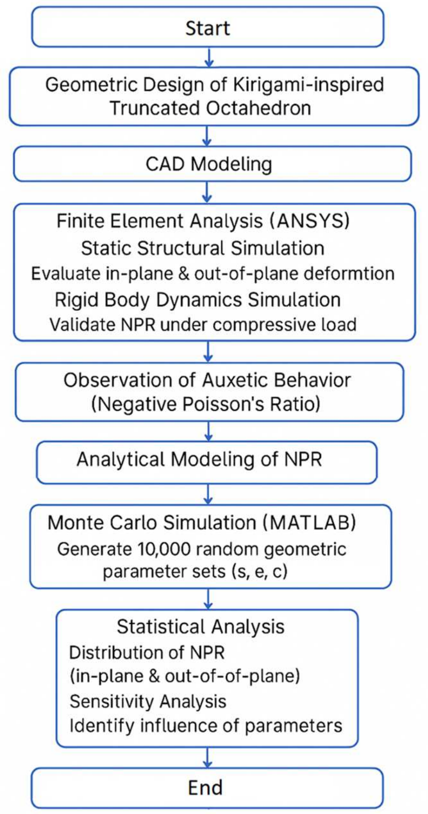

Fig. 4. Flowchart illustrating the stepwise methodology.

3. Governing Equations

We examine the unit cell's rigid origami motion by securing the six outer nodes of the bottom connector in the XY plane and applying a boundary condition for the longitudinal displacement to the top connector's outer node and confining their motion within the XY plane. For a vertical deformation δ applied to the geometric configuration, analytical expressions are derived for the angles α, β, and θ as functions of δ. The geometric relationships are expressed in Eqs. (1) to (3) [39]. The stochasticity is introduced by incorporating a variation parameter ($\bar{\omega}$):

$$\alpha = 2 \cdot \sin^{-1}\left(\frac{\sqrt{\left(\sqrt{6} - \frac{\delta}{s(\bar{\omega})}\right)^2 + 3}}{2\sqrt{3}} \right) \tag{1}$$

$$\beta = \sin^{-1}\left(\frac{\left(\sqrt{6} - \frac{\delta}{s(\bar{\omega})}\right)^2 - 3}{\sqrt{9 + 3\left(\sqrt{6} - \frac{\delta}{s(\bar{\omega})}\right)^2}} \right) \tag{2}$$

$$\theta = \sin^{-1}\left(\frac{2\left(\sqrt{6} - \frac{\delta}{s(\bar{\omega})}\right)}{\sqrt{9 + 3\left(\sqrt{6} - \frac{\delta}{s(\bar{\omega})}\right)^2}} \right) \tag{3}$$

The in-plane Poisson's ratio is expressed as [39]:

$$\nu_{zy} = \frac{\left(\left(\frac{2}{3}\sqrt{9 - \left(\sqrt{6} - \frac{\delta}{s(\bar{\omega})}\right)^2} - \frac{2}{\sqrt{3}} \right) - \frac{4e(\bar{\omega})}{s(\bar{\omega})} \left(\frac{\sqrt{2}}{3} - \frac{\sqrt{6} - \frac{\delta}{s(\bar{\omega})}}{\sqrt{9 + 3\left(\sqrt{6} - \frac{\delta}{s(\bar{\omega})}\right)^2}} \right) \right) \cdot \left(\frac{6c(\bar{\omega})}{s(\bar{\omega})} + 3\sqrt{6} \right)}{\frac{\delta}{s(\bar{\omega})}\left(5\sqrt{3} + \frac{e(\bar{\omega})}{s(\bar{\omega})} 4\sqrt{2} \right)} \tag{4}$$

The Out-of-the plane Poisson's ratio is expressed as [39]:

$$\nu_{zx} = \frac{\left(\left(\sqrt{9 - \left(\sqrt{6} - \frac{\delta}{s(\bar{\omega})}\right)^2} - \sqrt{3} \right) - \frac{2e(\bar{\omega})}{s(\bar{\omega})} \left(\sqrt{2} - \frac{6\left(\sqrt{6} - \frac{\delta}{s(\bar{\omega})}\right)}{\sqrt{9 + 3\left(\sqrt{6} - \frac{\delta}{s(\bar{\omega})}\right)^2}} \right) \right) \left(\frac{c(\bar{\omega})}{s(\bar{\omega})} + \sqrt{6} \right)}{\frac{\delta}{s(\bar{\omega})}\left(3\sqrt{3} + e(\bar{\omega}) 2\sqrt{2} \right)} \tag{5}$$

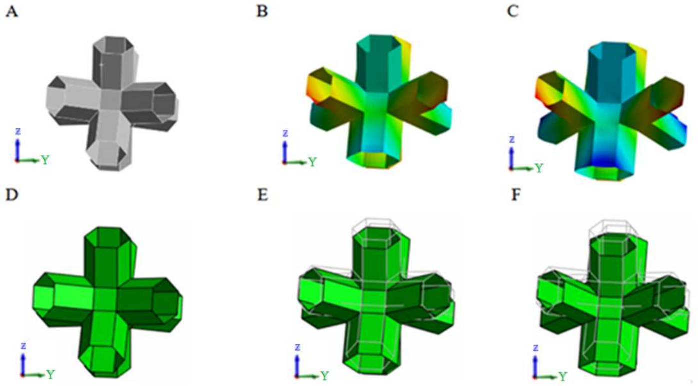

Fig. 5. Qualitative comparison of the deformation behavior considering a unit cell through finite element simulation and idealized structural simulation.

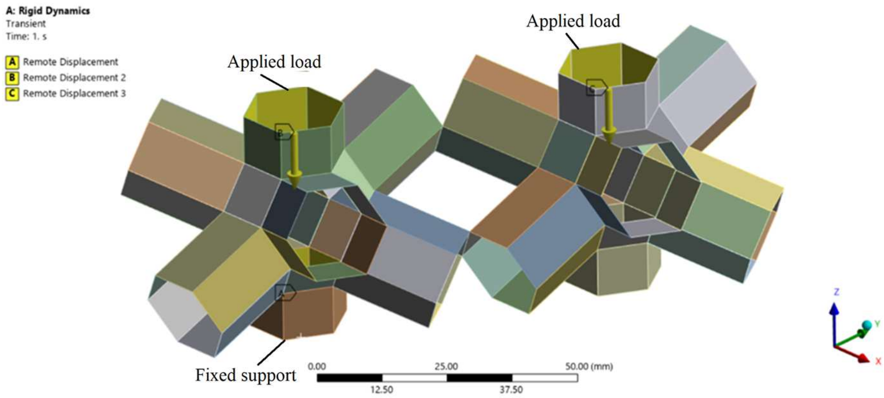

Fig. 6. Boundary conditions applied to the Kirigami geometry.

4. Results and Discussion

This section presents the outcomes from finite element simulations, rigid body dynamics, and analytical evaluations, offering a holistic understanding of the mechanical behavior of the proposed Kirigami-inspired metamaterial. The analysis emphasizes the auxetic performance under compressive loading, supported by both numerical simulations and theoretical predictions. A stochastic framework is also introduced to assess the sensitivity of auxetic behavior to geometric variations [59-63].

4.1. Static structural analysis of symmetric unit cell

The symmetric unit cell was subjected to uniaxial compressive loading in two increments–7000 N and 10,000 N–using a nonlinear static structural simulation in ANSYS. The geometry modeled as surface shell elements captures the deformation response while maintaining computational efficiency. Fig. 5 presents the qualitative deformation profiles obtained at each load level. Figure 5 A, and D represents undeformed stage obtained from the finite element simulations. Figure 5 B, and E represents deformed structure at 7000 N, while Fig. 5 C, and F represents deformed structure at 10,000 N.

The simulation revealed stress concentrations primarily around the junctions of extrusions and connectors, which could indicate potential failure zones under higher loads. The deformation pattern exhibited lateral expansion in response to axial compression, validating the auxetic behavior of the unit cell. These observations reinforce the suitability of the modified truncated octahedron geometry for mechanical metamaterial applications.

4.2. Rigid body dynamics: Auxetic validation through 2D tessellation

Figure 6 illustrates the applied boundary conditions for this simulation: fixed support at the bottom connector and force applied on the top edges. The mesh comprised quadrilateral shell elements, and the analysis incorporated geometric nonlinearity to accurately capture large deflection behavior. To verify the in-plane auxetic effect, a 2D tessellation composed of two rigid unit cells was analyzed using Rigid Body Dynamics in ANSYS. The model geometry utilized prismatic extrusions connected by revolute joints to simulate intercellular rotation, as typically seen in Kirigami-based structures.

Figure 7 illustrates the application of remote displacement boundary conditions for the rigid body dynamics simulation of a 2D Kirigami metamaterial tessellation. This simulation is aimed at evaluating the in-plane Poisson's ratio and understanding the directional deformation behavior under axial compression. The model uses revolute joints at each edge interface to simulate the kinematic freedom of the metamaterial structure, allowing realistic rotational movement during deformation. The key boundary conditions depicted in Fig. 7 are as follows:

Remote Displacement A: A fully fixed constraint is applied to the bottom-left connector of the tessellated structure. All degrees of freedom (translations and rotations in x, y, and z directions) are restricted. This serves as the anchor point, stabilizing the structure during compression.

Remote Displacement B: This is applied to the bottom-right connector. It is left unconstrained, allowing free motion. This freedom allows the structure to expand or contract laterally, thereby enabling the observation of auxetic response without artificially constraining deformation paths.

Remote Displacements C and D: A displacement of 10 mm in the negative Z-direction is imposed simultaneously on the top-left and top-right connectors of the unit cells. This mimics axial compressive loading and initiates the deformation process necessary to observe lateral expansion or contraction.

Remote Displacements E and F: These represent additional load points along the top edges, ensuring uniform distribution of the compressive force across the structure.

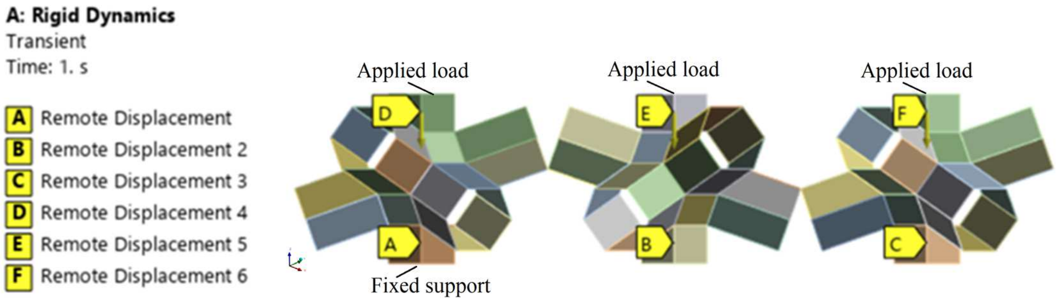

Fig. 7. Boundary conditions. Remote displacement A & C is free motion in xy plane and zero displacement in all other degrees of freedom. Remote displacement B is rigid support. Remote displacement D, E & F is displacement of 10 mm applied in negative z-direction.

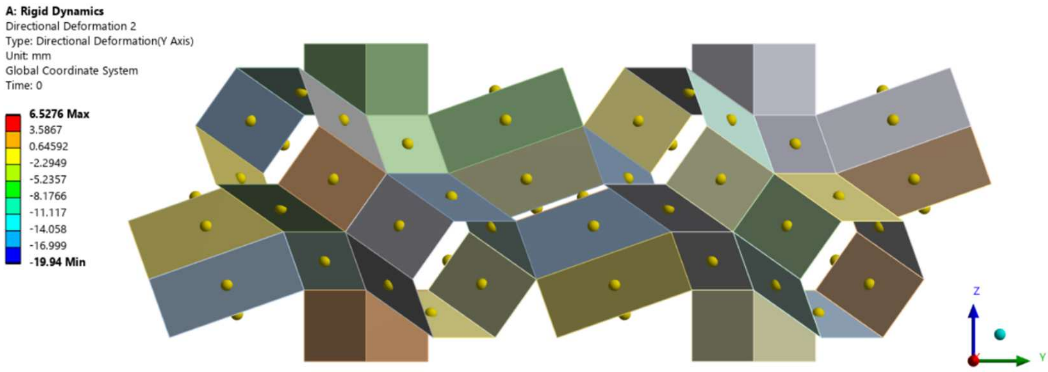

Fig. 8. Validation of auxetic nature of the 2D tessellation for undeformed model (the nodes are the centroids on each body at which the deformation results are calculated).

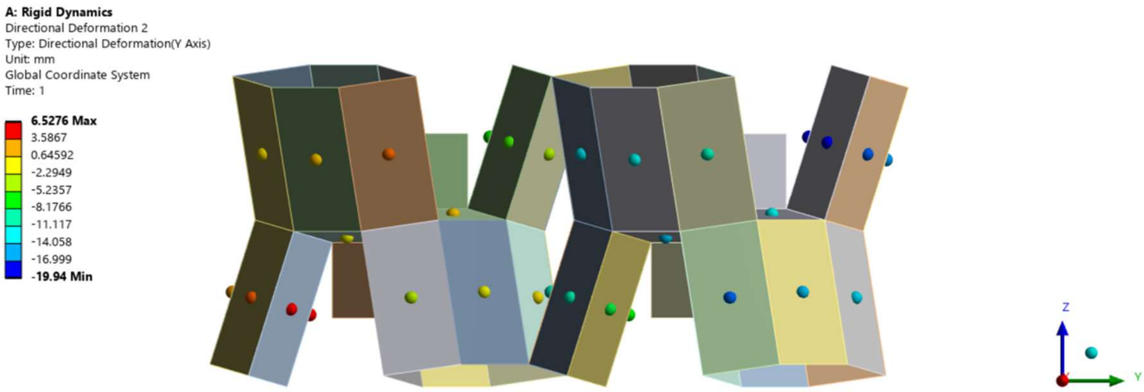

Fig. 9. Validation of auxetic nature of the 2D tessellation for directional deformation in y-direction.

For validation of in-plane Poisson's ratio of 2D Kirigami metamaterial, the geometry is modelled as surface body for each face and the revolute joints are used as connections between each contact edges. One connector at bottom of a unit cell is fixed and this boundary condition is applied using Remote Displacement with zero displacement in all degrees of freedom. The connector at the bottom of other unit cell is free to move and has no boundary conditions applied to it. A gradual displacement of 20 mm in negative Z-direction is applied on both top connectors on the tessellation using Remote Displacement boundary condition as shown in Fig. 7. Remote Displacement A – fixed support boundary condition applied to bottom left connector. Remote Displacement B and Remote Displacement C – displacement in negative z-direction applied to top left and right connectors.

ANSYS automatically assigns the centroids as the nodes for calculation of deformations for rigid bodies, as shown in the Fig. 8. The final deformed structure is shown in the Fig. 9, the rightmost nodes have displacement in the negative y-direction whereas the leftmost nodes have its displacement in the positive y-direction. Thus, the deformation results show that the structure compressed in the lateral direction when it is compressed in the longitudinal direction. The Poisson's ratio of the structure under the applied boundary conditions is calculated as below:

Displacement given in the z-direction = -20 mm;

Deformation of the structure in the z-direction (Δl) = -20 mm;

Deformation of the structure in the y-direction (Δy) = -19.94 mm - 6.5276 mm = -26.4676 mm;

Poisson's ratio in zy-direction (ν_{zy}) = (-Δy/y)/(Δl/l) = -0.5386.

The Poisson's ratio in zy-direction is negative which indicates that the structure is auxetic in nature in zy-direction.

4.3. Analytical validation and comparison with FEM

To further substantiate the numerical findings, analytical expressions were used to predict deformation and Poisson's ratio. Figure 10 displays the undeformed tessellated model, while Fig. 11 shows deformation due to axial loading. Figure 12 illustrates the relationship between Poisson's ratio and deformation magnitude for a unit cell with dimensions: Side length (*s*) = 10 mm, Extrusion length (*e*) = 20 mm, Connector length (*c*) = 20 mm. A strong agreement between analytical and finite element simulation results was observed.

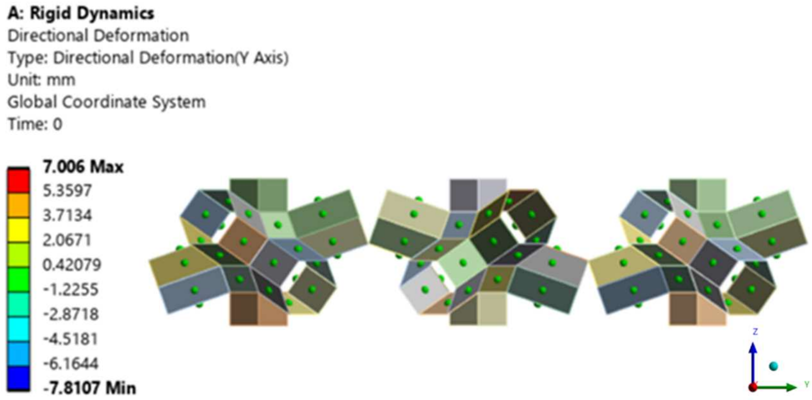

Fig. 10. Undeformed model.

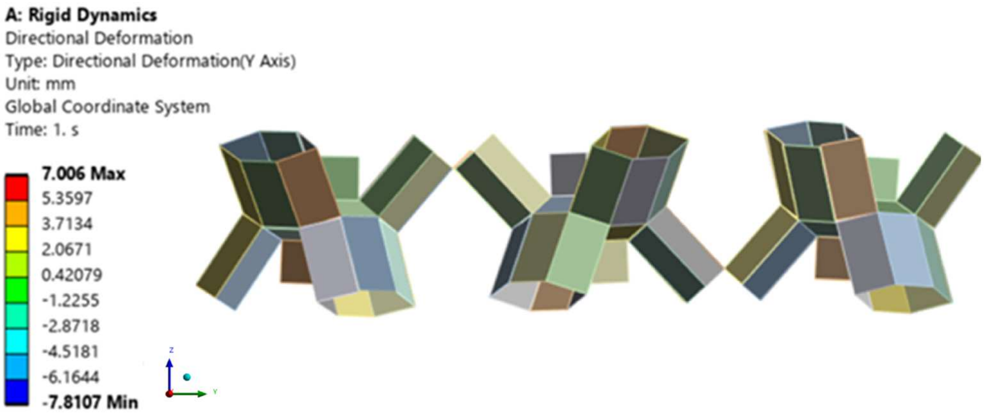

Fig. 11. Deformation due to compression.

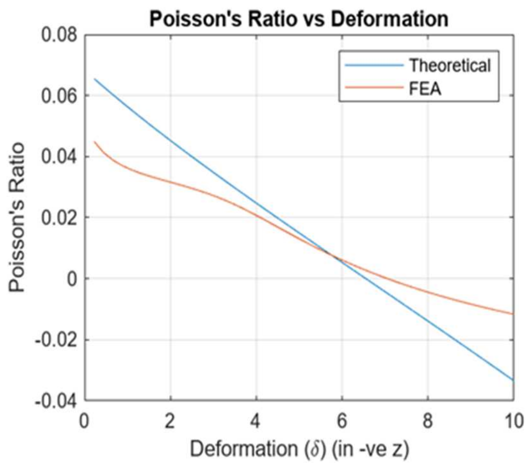

Fig. 12. Poisson’s Ratio vs Deformation of Unit Cell with s = 10 mm, e = 20 mm, and c = 20 mm.

The in-plane and out plane Poisson’s ratio are in close agreement with the published results, as presented in Table 3. It is important to note that the analytical formulation assumes ideal periodicity, whereas the FEM model inherently involves geometric edge effects due to the finite modeling domain. Nevertheless, the in-plane and out-of-plane Poisson’s ratios obtained from FEM (Table 3) show close agreement with both analytical and published results, validating the present approach. By definition, a single unit cell can represent the entire periodic structure when appropriate constraints or hinged interconnections are employed [56-58]. In this study, periodicity is conceptually maintained through hinged connections between neighbouring cells, ensuring uniform strain response across the lattice. Thus, the Kirigami structures can be simulated through finite element analysis which provide notable accuracy compared to analytical simulations. In addition, Fig. 13 represents the validation of the magnitude of angles (α, β and θ) predicted through analytical formulation with geometric configuration as s = 10 mm and as s = 20 mm, respectively. Figure 14 presents the correlation between Poisson's ratio and vertical deformation for extrusion length e = 20 mm, providing further insights into how the auxetic response evolves with geometric variation.

Table 3. Comparison of Poisson’s ratio with reference [39].

Poisson’s Ratio	Sinha and Mukhopadhyay [39]	FEM Results
In-plane	-0.204	-0.213
Out-of-plane	-0.127	-0.132

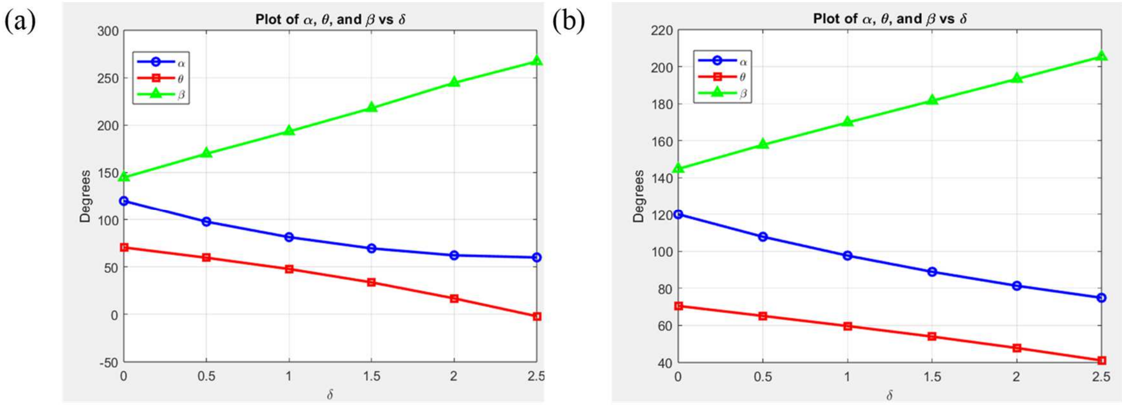

Fig. 13. Validation of magnitude of angles (α, β and θ) predicted through analytical formulation with geometric configuration as (a) s = 10 mm, (b) s = 20 mm.

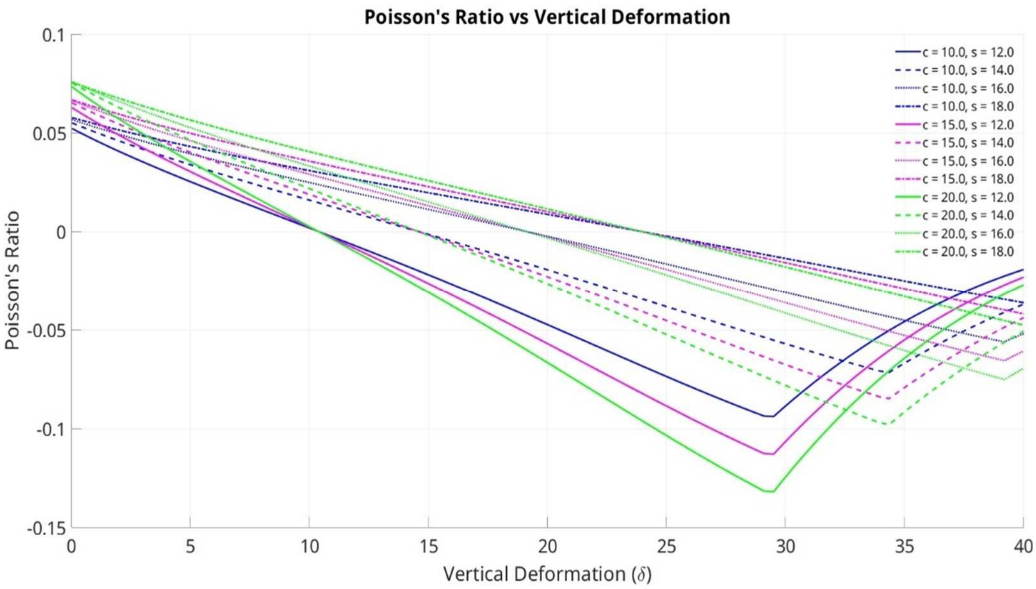

Fig. 14. Poisson's Ratio vs Vertical Deformation at e = 20 mm.

4.4. Deterministic and stochastic analysis

To statistically validate the NPR behavior, MATLAB is used to implement the Monte Carlo method. Geometric parameters are varied across 10,000 samples within predefined ranges, ensuring comprehensive coverage of the design space. For each sample, the NPR is calculated based on the deformation characteristics derived from analytical formulations. The results are compiled into a probability distribution curve to identify trends and sensitivities. Initially, deformation parameters such as α, β and θ are calculated based on vertical deformation (δ) and side length (s) using customized equations. These parameters are plotted to analyse their behavior with varying δ, providing insights into the angular deformations of the structure. For a deeper exploration, Poisson's Ratio (v) is analytically formulated to study its relationship with deformation and geometric factors (s, c, and e) under various conditions. The curves generated for multiple combinations of these parameters, offering a visualization of how material behavior changes with design and material constants as shown in Fig. 13. In Fig. 14, the Poisson's ratio is first positive for the lower values of vertical deformation (compression) and becomes negative with increase in the deformation until the structure gets contacted within itself, thus it gives rise a steep increase in the Poisson's ratio.

The set of plots in Fig. 15 illustrates the sensitivity analysis of the in-plane Poisson's ratio under variations of three key geometric parameters: connector length (c), extrusion length (e), and side length (s). Each subfigure represents the probability density distribution of the in-plane Poisson's ratio when one or more geometric parameters are perturbed by ±5%, ±10%, and ±15%. Figure 15 (a) depicts the effect of varying connector length (c = 20 mm). As the variation increases from ±5% to ±15%, the probability density function (PDF) broadens and flattens, indicating a wider range of possible Poisson's ratio outcomes. This signifies that larger deviations in connector length increase uncertainty in the in-plane Poisson's ratio, though the peak remains centered close to –0.21, suggesting limited influence in shifting the mean value. Figure 15 (b) explores the variation in extrusion length (e = 20 mm). Similar to connector length, increasing variation from ±5% to ±15% results in a broader distribution. However, the peak of the distribution shifts more noticeably compared to Fig. 16(a), indicating that extrusion length has a stronger effect on both the variability and the central value of the in-plane Poisson's ratio. Figure 15 (c) shows the sensitivity to changes in side length (s = 10 mm). The distributions are significantly broader and less sharply peaked compared to the previous two parameters. The distribution spreads from approximately –0.5 to +0.1 for the ±15% case, implying that side length has a substantial impact on the in-plane Poisson's ratio and introduces high variability, even leading to sign change in some cases (from negative to slightly positive values). Figure 15 (d) represents the cumulative effect when all three parameters are varied simultaneously by ±5%, ±10%, and ±15%. The combined variations produce an even broader distribution compared to any individual parameter change, suggesting strong interactions among the parameters and compounding uncertainty in the Poisson's response. Figure 15 (e) compares the influence of each parameter individually at a fixed ±10% variation. The sharpest peak is observed for connector length, indicating the least variability, followed by extrusion length, and the widest distribution is observed for side length, again confirming that side length introduces the most sensitivity in the in-plane Poisson's ratio.

Table 4. Sensitivity Indices for In-plane Poisson's ratio.

Stochastic variability parameter	Sensitivity Indices			
	Connector length (*c*)	Extrusion length (*e*)	Side length (*s*)	Deformation (δ)
±5%	0.0451	0.2399	0.4995	0.2155
±10%	0.0455	0.2402	0.4986	0.2157
±15%	0.0456	0.2473	0.489	0.218

Table 5. Sensitivity Indices for Out-of-plane Poisson's ratio.

Stochastic variability parameter	Sensitivity Indices			
	Connector length (*c*)	Extrusion length (*e*)	Side length (*s*)	Deformation (δ)
±5%	0.0138	0.0509	0.4971	0.4382
±10%	0.0141	0.0514	0.4813	0.4532
±15%	0.0142	0.0521	0.4609	0.4728

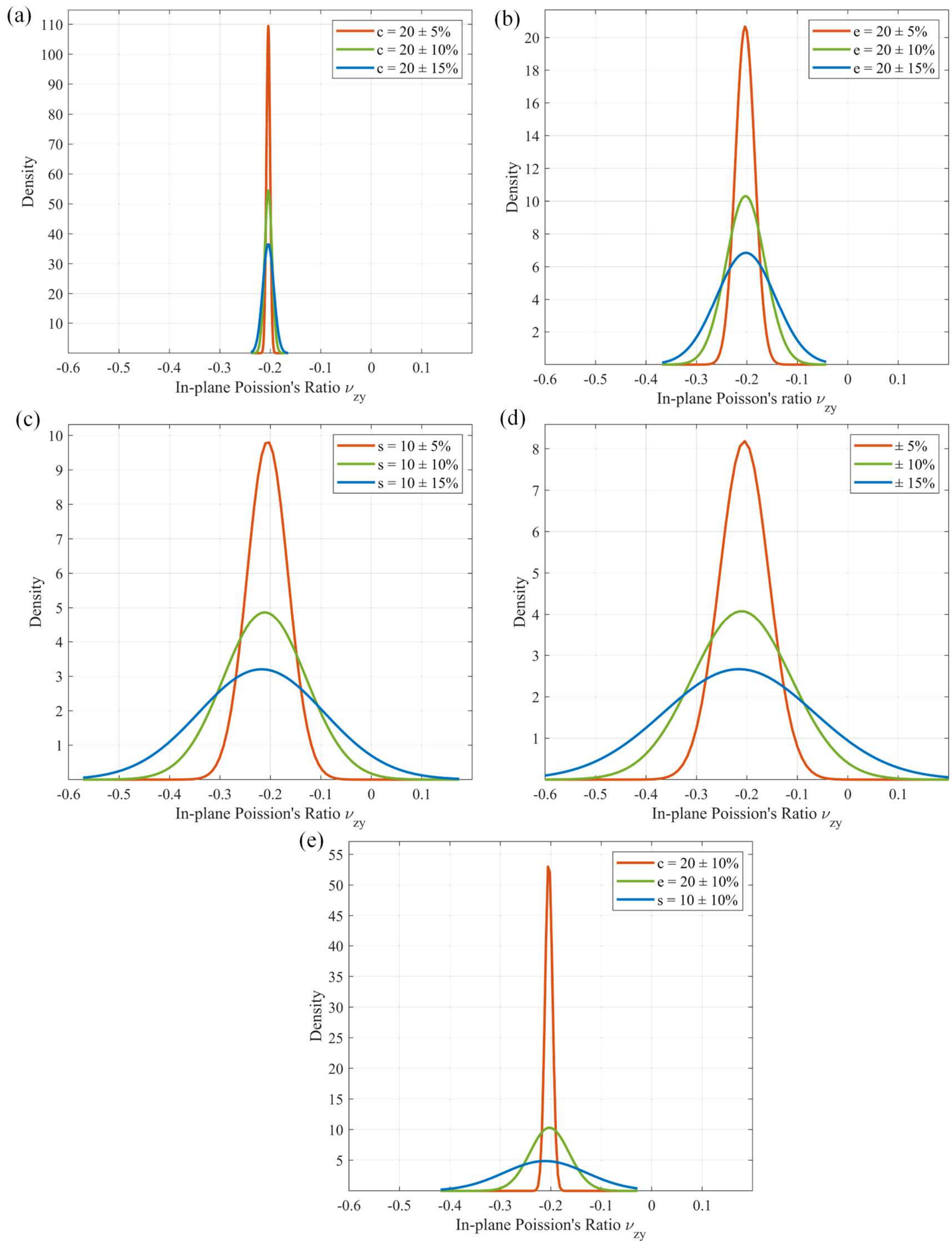

Fig. 15. (a) Normal distribution of ν_{zy} with variability of 'c', (b) Normal distribution of ν_{zy} with variability of 'e', (c) Normal distribution of ν_{zy} with variability of 's', (d) Normal distribution of ν_{zy} with variability of all parameters simultaneously, (e) Normal distribution of ν_{zy} with variability of 'c', 'e' and 's'.

Figure 16 presents a detailed probabilistic sensitivity analysis of the out-of-plane Poisson's ratio by evaluating the effects of geometric parameter variations—connector length (c), extrusion length (e), and side length (s)—within ±5%, ±10%, and ±15% bounds. In Fig. 16 (a), variations in connector length show a relatively narrow distribution, with the peak consistently around –0.127, indicating a small and stable influence on the out-of-plane Poisson's ratio even under increased perturbations. Figure 16 (b) displays the effect of extrusion length variations, with broader distributions compared to (a), suggesting that extrusion length introduces more variability and a modest shift in the Poisson's response. Figure 16 (c) demonstrates that side length variations have a substantial impact, with significantly wider distributions and even a range that crosses zero, implying possible sign changes in the out-of-plane Poisson's ratio and highlighting high sensitivity. Figure 16 (d) shows the combined effect of simultaneous variation in all three parameters, resulting in a markedly broader distribution, emphasizing the compounded uncertainty due to parameter interactions. Finally, Fig. 16 (e) compares the impact of a fixed ±10% variation in each parameter, revealing that connector length results in the most concentrated distribution (sharpest peak), extrusion length causes moderate spread, and side length exhibits the widest spread with lower peak values. These observations confirm that while connector length (c) has the least influence, side length (s) dominates the sensitivity of the out-of-plane Poisson's ratio, followed by extrusion length (e), consistent with the trends in Table 5.

4.3. Sensitivity analysis

Tables 4 and 5 present the sensitivity indices for in-plane and out-of-plane Poisson's ratios, respectively, highlighting how variations in key geometric parameters influence the mechanical response of the Kirigami-based metamaterial. In Table 4, the in-plane Poisson's ratio is most sensitive to changes in side length (s), which consistently shows the highest sensitivity index across all perturbation levels (0.4995 at ±5%, 0.4986 at ±10%, and 0.4890 at ±15%), indicating that even small variations in side length significantly affect the in-plane auxetic response. Extrusion length (e) and deformation (δ) also show moderate influence, with indices around 0.24 and 0.215, respectively, suggesting their secondary yet notable contribution. In contrast, connector length (c) exhibits a very low sensitivity index (around 0.045), implying minimal impact on the in-plane response. This implies that structural tuning for in-plane behavior should prioritize side length and extrusion adjustments.

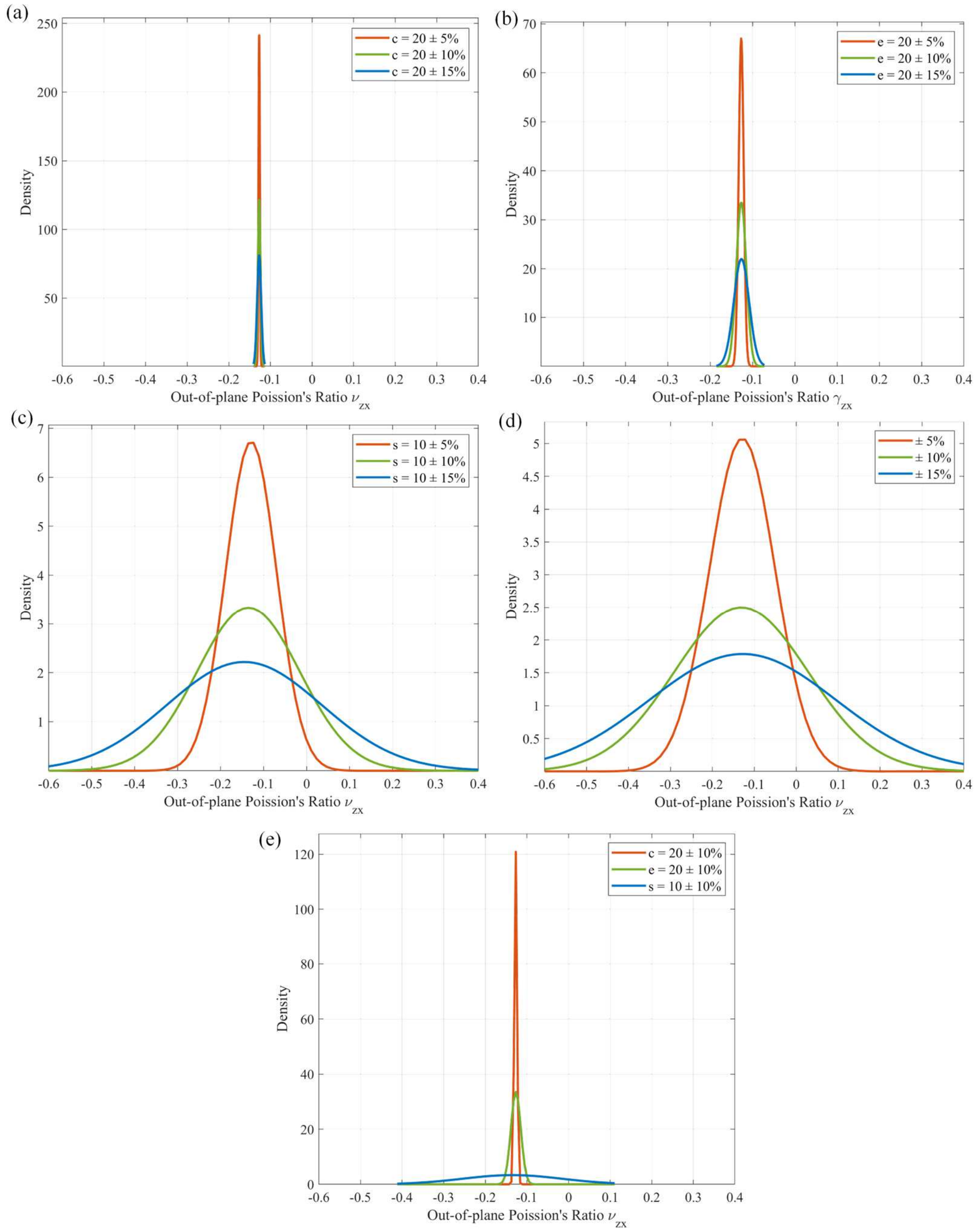

Fig. 16. (a) Normal distribution of ν_{zx} with variability of 'c', (b) Normal distribution of ν_{zx} with variability of 'e', (c) Normal distribution of ν_{zx} with variability of 's', (d) Normal distribution of ν_{zx} with variability of all parameters simultaneously, (e) Normal distribution of ν_{zx} with variability of 'c', 'e' and 's'.

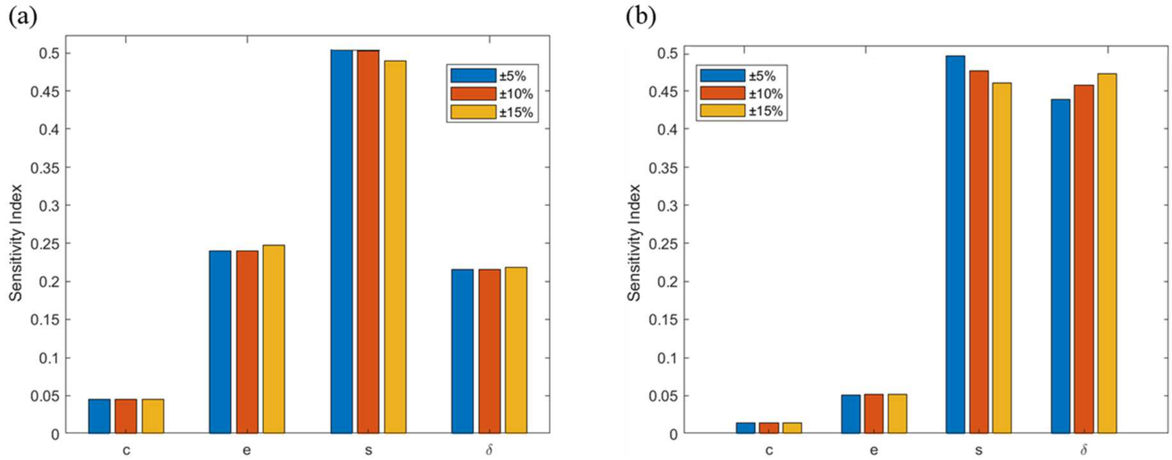

Fig. 17. Sensitivity indices of geometric parameters for (a) in-plane and (b) out-of-plane Poisson's ratios under different perturbation levels (±5%, ±10%, and ±15%). Blue, orange, and yellow bars represent the respective perturbation magnitudes.

In Table 5, which focuses on out-of-plane Poisson's ratio, the pattern shifts notably: deformation (δ) and side length (s) dominate the response, with δ's sensitivity increasing from 0.4382 at ±5% to 0.4728 at ±15%, and s maintaining a relatively high index, though slightly decreasing from 0.4971 to 0.4609. These results underscore that deformation mechanisms and vertical geometry largely govern the out-of-plane auxetic behavior. Meanwhile, both extrusion length (e) and connector length (c) show minimal influence, with their indices remaining below 0.053 across all variations. Collectively, the sensitivity analysis confirms that side length is a critical parameter influencing both in-plane and out-of-plane auxeticity, while deformation (δ) is particularly crucial for tuning out-of-plane response. These insights can guide precise geometric tailoring for optimized auxetic performance in Kirigami-inspired metamaterials.

The influence of key geometric parameters on the auxetic behavior of the Kirigami metamaterial is further illustrated in Fig. 17. The color-coded bar plots represent the sensitivity indices corresponding to three perturbation levels (±5%, ±10%, and ±15%), where blue, orange, and yellow bars denote each perturbation level, respectively. This visual representation provides a clear comparative understanding of how parameter variations affect the auxetic response. The consistent dominance of side length (s) and deformation (δ) across all perturbations reinforces their significance in optimizing the structural performance of the proposed metamaterial.

5. Conclusion

This study presented a comprehensive investigation into the auxetic behavior of a truncated octahedron-based Kirigami mechanical metamaterial using a hybrid approach combining finite element simulations, analytical modeling, and stochastic analysis. Through static structural and rigid body dynamics simulations in ANSYS, the unit cell and its tessellated assembly are analysed under compressive loading to validate their negative Poisson's ratio (NPR) characteristics. The simulations confirmed lateral expansion under axial compression—a hallmark of auxetic materials—demonstrating both in-plane and out-of-plane NPR behavior. The numerical results are found to be in strong agreement with theoretical predictions, confirming the robustness of the geometric design in producing auxetic effects. To extend the deterministic findings, a Monte Carlo-based stochastic analysis is conducted in MATLAB, generating 10,000 random samples by perturbing key geometric parameters—side length (s), extrusion length (e), and connector length (c). This enabled statistical validation of NPR behavior and quantified the effects of parameter variability. The probabilistic sensitivity analysis revealed that side length (s) plays the most influential role in both in-plane and out-of-plane NPR responses, followed by deformation (δ) and extrusion length (e), whereas connector length (c) had minimal impact. These insights are further supported by variance-based global sensitivity indices. The dual-mode auxetic behavior and its tunability through geometric design provide a significant advancement in the development of flexible, energy-absorbing, and impact-resistant metamaterials. This work offers a robust design framework that integrates CAD modeling, finite element simulations, and statistical analysis, paving the way for engineering next-generation multifunctional metamaterials. Future work could explore the dynamic response under time-varying loads, material anisotropy, and real-world fabrication constraints to further harness the potential of Kirigami-inspired auxetic structures.

Author contributions

S.B. Naidu, Y. Kamasani, and S. Dey conceived the idea; S.B. Naidu, Y. Kamasani, and S. Barman performed the simulations and prepared the initial draft; S. Barman and S. Dey contributed significantly to the preparation and finalization of the manuscript. The manuscript was written through the contribution of all authors. All authors discussed the results, reviewed, and approved the final version of the manuscript.

Acknowledgments

The authors would like to extend their sincere gratitude to the Uncertainty Quantification (UQ) Lab, Department of Mechanical Engineering, NIT Silchar, for granting access to the computational facilities.

Conflict of Interest

The authors declared no potential conflicts of interest concerning the research, authorship, and publication of this article.

Funding

The authors received no financial support for the research, authorship, and publication of this article.

Data Availability Statements

The datasets generated and/or analyzed during the current study are available from the corresponding author on reasonable request.

Nomenclature

s	Side length [mm]	β	Angle between a square panel and an adjacent prismatic extrusion [degree]
e	Extrusion length [mm]	θ	Angle between a prismatic extrusion and a connector [degree]
c	Connector length [mm]	ν_{zy}	In-plane Poisson's ratio (lateral contraction in y due to z compression)
δ	Vertical displacement [mm]	ν_{zx}	Out-of-plane Poisson's ratio (lateral contraction in x due to z compression)
α	Angle between the highlighted edges of the prismatic extrusions [degree]	$\bar{\omega}$	Variation parameter

References

[1] Zheludev, N.I., Kivshar, Y.S., From metamaterials to metadevices, *Nature Materials*, 11(11), 2012, 917-924.
[2] Cui, T.J., Smith, D.R., Liu, R., *Metamaterials*, Springer, New York, 2010.
[3] Kadic, M., Milton, G.W., van Hecke, M., Wegener, M., 3D metamaterials, *Nature Reviews Physics*, 1(3), 2019, 198-210.
[4] Liu, Y., Zhang, X., Metamaterials: a new frontier of science and technology, *Chemical Society Reviews*, 40(5), 2011, 2494-2507.
[5] Engheta, N., Ziolkowski, R.W. (Eds.), *Metamaterials: Physics and Engineering Explorations*, John Wiley & Sons, 2006.
[6] Zadpoor, A.A., Mechanical meta-materials, *Materials Horizons*, 3(5), 2016, 371-381.
[7] Munk, B.A., *Metamaterials: Critique and Alternatives*, John Wiley & Sons, 2009.
[8] Barchiesi, E., Spagnuolo, M., Placidi, L., Mechanical metamaterials: a state of the art, *Mathematics and Mechanics of Solids*, 24(1), 2019, 212-234.
[9] Kshetrimayum, R.S., A brief intro to metamaterials, *IEEE Potentials*, 23(5), 2004, 44-46.
[10] Kadic, M., Milton, G.W., van Hecke, M., Wegener, M., 3D metamaterials, *Nature Reviews Physics*, 1(3), 2019, 198-210.
[11] Kadic, M., Bückmann, T., Schittny, R., Wegener, M., Metamaterials beyond electromagnetism, *Reports on Progress in Physics*, 76(12), 2013, 126501.
[12] Tong, X.C., *Functional Metamaterials and Metadevices*, Vol. 262, Springer, Bolingbrook, IL, 2018.
[13] Singh, G., A review of metamaterials and its applications, *International Journal of Engineering Trends and Technology*, 19(6), 2015, 305-310.
[14] Chen, T., Li, S., Sun, H., Metamaterials application in sensing, *Sensors*, 12(3), 2012, 2742-2765.
[15] Valipour, A., Kargozarfard, M.H., Rakhshi, M., Yaghootian, A., Sedighi, H.M., Metamaterials and their applications: an overview, *Proceedings of the Institution of Mechanical Engineers, Part L: Journal of Materials: Design and Applications*, 236(11), 2022, 2171-2210.
[16] Capolino, F., *Applications of Metamaterials*, CRC Press, 2017.
[17] Surjadi, J.U., Gao, L., Du, H., Li, X., Xiong, X., Fang, N.X., Lu, Y., Mechanical metamaterials and their engineering applications, *Advanced Engineering Materials*, 21(3), 2019, 1800864.
[18] Krzysztofik, W.J., Cao, T.N., Metamaterials in application to improve antenna, *Metamaterials and Metasurfaces*, 2019, 63.
[19] Wu, F., Zheng, C., Wei, Y., Xue, X., Liao, J., Current progress of acoustic metastructures: design strategy and prospective application, *Advanced Engineering Materials*, 2024, 2402910.
[20] Aydın, G., San, S.E., Breaking the limits of acoustic science: a review of acoustic metamaterials, *Materials Science and Engineering: B*, 305, 2024, 117384.
[21] Gu, X., Wang, L., Guan, X., Wang, Y., Cheng, Y., Wu, Y., Advances in the design, preparation and application of biomimetic damping materials, *Giant*, 2024, 100321.
[22] Li, X., Gao, L., Zhou, W., Wang, Y., Lu, Y., Novel 2D metamaterials with negative Poisson's ratio and negative thermal expansion, *Extreme Mechanics Letters*, 30, 2019, 100498.
[23] Qin, H., Yang, D., Ren, C., Modelling theory of functional element design for metamaterials with arbitrary negative Poisson's ratio, *Computational Materials Science*, 150, 2018, 121-133.
[24] Li, F., Zhang, Q., Shi, H., Liu, Z., A modified three-dimensional negative-Poisson-ratio metal metamaterial lattice structure, *Materials*, 15(11), 2022, 3752.
[25] Li, F., Zhang, Q., Wang, Z., Zhu, D., A new three-dimensional re-entrant negative Poisson's ratio metamaterial with tunable stiffness, *Engineering Structures*, 306, 2024, 117793.
[26] Guo, C., Zhao, D., Liu, Z., Ding, Q., Gao, H., Yan, Q., Sun, Y., Ren, F., The 3D-printed honeycomb metamaterial tubes with tunable negative Poisson's ratio for high-performance static and dynamic mechanical properties, *Materials*, 14(6), 2021, 1353.
[27] Ren, X., Das, R., Tran, P., Ngo, T.D., Xie, Y.M., Auxetic metamaterials and structures: a review, *Smart Materials and Structures*, 27(2), 2018, 023001.
[28] Kolken, H.M., Zadpoor, A.A., Auxetic mechanical metamaterials, *RSC Advances*, 7(9), 2017, 5111-5129.
[29] Wang, Z., Luan, C., Liao, G., Liu, J., Yao, X., Fu, J., Progress in auxetic mechanical metamaterials: structures, characteristics, manufacturing methods, and applications, *Advanced Engineering Materials*, 22(10), 2020, 2000312.
[30] Gatt, R., Mizzi, L., Azzopardi, J.I., Azzopardi, K.M., Attard, D., Casha, A., Briffa, J., Grima, J.N., Hierarchical auxetic mechanical metamaterials, *Scientific Reports*, 5(1), 2015, 8395.
[31] Han, D., Ren, X., Zhang, Y., Zhang, X.Y., Zhang, X.G., Luo, C., Xie, Y.M., Lightweight auxetic metamaterials: design and characteristic study, *Composite Structures*, 293, 2022, 115706.
[32] Grima, J.N., Caruana-Gauci, R., Dudek, M.R., Wojciechowski, K.W., Gatt, R., Smart metamaterials with tunable auxetic and other properties, *Smart Materials and Structures*, 22(8), 2013, 084016.
[33] Luo, C., Han, C.Z., Zhang, X.Y., Zhang, X.G., Ren, X., Xie, Y.M., Design, manufacturing and applications of auxetic tubular structures: a review, *Thin-Walled Structures*, 163, 2021, 107682.
[34] Mousanezhad, D., Babaee, S., Ebrahimi, H., Ghosh, R., Hamouda, A.S., Bertoldi, K., Vaziri, A., Hierarchical honeycomb auxetic metamaterials, *Scientific Reports*, 5(1), 2015, 18306.
[35] He, Y., Bi, Z., Wang, T., Wang, L., Lu, G., Cui, Y., Tse, K.M., Design and mechanical properties analysis of hexagonal perforated honeycomb metamaterial, *International Journal of Mechanical Sciences*, 270, 2024, 109091.
[36] Zhang, P.F., Qie, Y.H., Li, N.N., Song, J.H., A novel auxetic metamaterial based on SSH with unique enhanced load-bearing capacity and NPR effect, *Mechanics of Advanced Materials and Structures*, 2025, 1-23.
[37] Wang, S., Deng, C., Ojo, O., Akinrinlola, B., Kozub, J., Wu, N., Design and modeling of a novel three-dimensional auxetic reentrant honeycomb structure for energy absorption, *Composite Structures*, 280, 2022, 114882.
[38] Dong, Z., Li, Y., Zhao, T., Wu, W., Xiao, D., Liang, J., Experimental and numerical studies on the compressive mechanical properties of the metallic auxetic reentrant honeycomb, *Materials & Design*, 182, 2019, 108036.
[39] Sinha, A., Mukhopadhyay, T., Kirigami-inspired metamaterials for programming constitutive laws: mixed-mode multidirectional auxeticity and contact-induced stiffness modulation, *iScience*, 25(12), 2022.
[40] Zhang, W., Yin, H., Wu, Y., Jin, Q., Wu, L., Wen, G., Liu, J., Wu, X., A novel auxetic 3D lattice structure for enhancing energy absorption, *Composite Structures*, 326, 2023, 117620.
[41] Tang, Y., Lin, G., Yang, S., Yi, Y.K., Kamien, R.D., Yin, J., Programmable kiri-kirigami metamaterials, *Advanced Materials*, 29(10), 2017, 1604262.

[42] Sun, Y., Ye, W., Chen, Y., Fan, W., Feng, J., Sareh, P., Geometric design classification of kirigami-inspired metastructures and metamaterials, *Structures*, 33, 2021, 3633-3643.
[43] Zhang, H., Paik, J., Kirigami design and modeling for strong, lightweight metamaterials, *Advanced Functional Materials*, 32(21), 2022, 2107401.
[44] Li, Y., Zhang, Q., Hong, Y., Yin, J., 3D transformable modular kirigami-based programmable metamaterials, *Advanced Functional Materials*, 31(43), 2021, 2105641.
[45] Dureisseix, D., An overview of mechanisms and patterns with origami, *International Journal of Space Structures*, 27(1), 2012, 1-14.
[46] Chen, S.H., Chan, K.C., Han, D.X., Zhao, L., Wu, F.F., Programmable super elastic kirigami metallic glasses, *Materials & Design*, 169, 2019, 107687.
[47] Li, Y., Yin, J., Metamorphosis of three-dimensional kirigami-inspired reconfigurable and reprogrammable architected matter, *Materials Today Physics*, 21, 2021, 100511.
[48] Hou, Y., Tai, Y.H., Lira, C., Scarpa, F., Yates, J.R., Gu, B., The bending and failure of sandwich structures with auxetic gradient cellular cores, *Composites Part A: Applied Science and Manufacturing*, 49, 2013, 119-131.
[49] Qiu, H., Feng, Y., Gao, Y., Hong, Z., Tan, J., Gradient design and fabrication methodology for interleaved self-locking kirigami panels, *Computer-Aided Design*, 166, 2024, 103632.
[50] Ruan, B., Zhang, L., Dou, W., Zhang, D., Stichel, S., Experiments and design of a kirigami-based multi-stage energy absorption structure subjected to axial impact, *Thin-Walled Structures*, 200, 2024, 111920.
[51] Lu, C., Li, R., Zheng, Y., Pan, F., Chen, Y., Zhang, X., The deployment of 3-D morphing surfaces: a 2-D auxetic metamaterial approach through buckling-induced mechanism, *Composite Structures*, 348, 2024, 118432.
[52] Wang, H., Zhao, D., Jin, Y., Wang, M., Mukhopadhyay, T., You, Z., Modulation of multi-directional auxeticity in hybrid origami metamaterials, *Applied Materials Today*, 20, 2020, 100715.
[53] Wei, Z., Wu, Y., Lai, H., Qian, J., Compression-twist coupling mechanical metamaterials with programmed bistability, *Acta Mechanica Solida Sinica*, 2025, 1-9.
[54] Yin, X., Gao, Z.Y., Zhang, S., Zhang, L.Y., Xu, G.K., Truncated regular octahedral tensegrity-based mechanical metamaterial with tunable and programmable Poisson's ratio, *International Journal of Mechanical Sciences*, 167, 2020, 105285.
[55] Chen, Y., Ye, W., Xu, R., Sun, Y., Feng, J., Sareh, P., A programmable auxetic metamaterial with tunable crystal symmetry, *International Journal of Mechanical Sciences*, 249, 2023, 108249.
[56] Gibson, L.J., Cellular solids, *MRS Bulletin*, 28(4), 2003, 270-274.
[57] Masters, I.G., Evans, K.E., Models for the elastic deformation of honeycombs, *Composite Structures*, 35(4), 1996, 403-422.
[58] Wang, H., Zhao, D., Jin, Y., Wang, M., Mukhopadhyay, T., You, Z., Modulation of multi-directional auxeticity in hybrid origami metamaterials, *Applied Materials Today*, 20, 2020, 100715.
[59] Barman, S., Deka, J., Dey, S., Exploring Stochastic Surface and Structural Characteristics in 3D-Printed Polymer Parts Using a Digital Twin Approach, *Journal of Advanced Manufacturing Systems*, 2025, 1-23.
[60] Barman, S., Gupta, K.K., Kushari, S., Dey, S., Stochastic performance of journal bearing with two-layered porous bush—A machine learning approach, *Journal of Tribology*, 145(10), 2023, 104101.
[61] Vaishali, Kushari, S., Kumar, R.R., Karsh, P.K., Dey, S., Sensitivity analysis of random frequency responses of hybrid multi-functionally graded sandwich shells, *Journal of Vibration Engineering & Technologies*, 11(3), 2023, 845-872.
[62] Kushari, S., Mukhopadhyay, T., Chakraborty, A., Maity, S.R., Dey, S., Probability-based unified sensitivity analysis for multi-objective performances of composite laminates: a surrogate-assisted approach, *Composite Structures*, 294, 2022, 115559.
[63] Vaishali, Dey, S., *Support vector model based thermal uncertainty on stochastic natural frequency of functionally graded cylindrical shells*, In Recent Advances in Computational Mechanics and Simulations: Volume-I: Materials to Structures, Singapore: Springer Singapore, 2020.

ORCID iD

Subrata Barman https://orcid.org/0000-0002-5400-0079
Simma Bhargava Naidu https://orcid.org/0009-0002-7620-5523
Yashwanth Kamasani https://orcid.org/0009-0001-1241-7415
Sudip Dey https://orcid.org/0000-0002-0453-7329

How to cite this article: Barman S., et al., Transfiguration of Random Auxeticity of Programmable Metamaterial: A Kirigami inspired approach, *J. Appl. Comput. Mech.*, xx(x), 2025, 1–13. https://doi.org/10.22055/jacm.2025.48638.5385